



## Full Text View

[Volume 29, Issue 7 \(July 1999\)](#)

## Journal of Physical Oceanography

 Article: pp. 1528–1541 | [Abstract](#) | [PDF \(848K\)](#)

## Evolution of Interdecadal Variability in Sea Level Pressure, Sea Surface Temperature, and Upper Ocean Temperature over the Pacific Ocean\*

**Yves M. Tourre and Yochanan Kushnir**
*Lamont-Doherty Earth Observatory, Columbia University, Palisades, New York*
**Warren B. White**
*Scripps Institute of Oceanography, University of California, San Diego, La Jolla, California*

(Manuscript received June 6, 1997, in final form July 28, 1998)

DOI: 10.1175/1520-0485(1999)029&lt;1528:EOIVIS&gt;2.0.CO;2

## ABSTRACT

Interdecadal variability in sea level pressure (SLP) and sea surface temperature (SST) anomalies in the Pacific Ocean was “quasiperiodic” from 1900–91. The coherent variability of this phenomenon is investigated using gridded observational data from the turn of the century (SST and SLP) and of upper ocean heat content (HS) from the recent two and a half decades. The nominal cycle in atmosphere–ocean variables is roughly two decades long, but growth and decay can happen on a shorter timescale (e.g., half a cycle or so). The authors divide the full cycle into four phases: An onset phase, during which a weak SLP anomaly pattern off Japan takes approximately 2–4 yr to expand eastward, leads to large SLP anomalies in the region of the Aleutian low. A quasi-stationary growth phase, with the midlatitude SLP anomaly pattern in the eastern ocean, intensifies over a 2–4-yr period. The persistent SLP anomalies evolve in concert with large SST (and HS anomalies) of the same polarity located to the south-southwest along the subarctic frontal zone (SAFZ). During the growth phase, SST anomalies with opposite polarity develop to the east, associated with anomalous atmospheric circulation along the North American coastline. Near the end of the growth phase a narrow tongue of enhanced SST anomalies is found along the subtropical front near Hawaii, slightly to the west of the subduction region associated with the subtropical gyre. Following is a decay phase during which the midocean SST and SLP anomalies weaken, while the HS anomalies persist in the southern part of the subtropical gyre. Concomitantly, a weak anomalous east–west SLP gradient is established in the tropical Pacific and could contribute to the interdecadal variability of the southern oscillation index. Finally, a return phase occurs (identical to the onset phase but with opposite polarity), during which SST anomalies move from the Alaskan gyre

## Table of Contents:

- [Introduction](#)
- [Data and methods](#)
- [Results](#)
- [Discussion and conclusions](#)
- [REFERENCES](#)
- [FIGURES](#)

## Options:

- [Create Reference](#)
- [Email this Article](#)
- [Add to MyArchive](#)
- [Search AMS Glossary](#)

## Search CrossRef for:

- [Articles Citing This Article](#)

## Search Google Scholar for:

- [Yves M. Tourre](#)
- [Yochanan Kushnir](#)
- [Warren B. White](#)

and from the center of the subtropical gyre to merge onto the SAFZ. During the evolution of the interdecadal phenomenon, the overall structure of HS highlights the notion that the subtropical gyre integrates the thermal and dynamical forcing induced by the persistent surface circulation anomaly. Since only the oceanic anomalies retain their character throughout the seasonal cycle, the interdecadal phenomenon may owe its existence to coupled ocean–atmosphere interaction in which ocean surface anomalies feed back on the atmosphere providing the necessary links between consecutive winter seasons. It is suggested that this can occur through interactions in either midlatitudes (delayed-negative feedback) and/or the Tropics.

## 1. Introduction

Evidence of low-frequency variability and trends in the global sea surface temperature (SST) record have received attention in recent literature (e.g., [Folland et al. 1984](#); [Oort et al. 1987](#); [Kawamura 1994](#); [White and Cayan, 1998](#)). Using complex singular value decomposition in the frequency domain, [Mann et al. \(1995\)](#) were able to show the presence of a significant signal with a 15–25-yr period in the global SST record over the past century and a half. Additional analyses of historical datasets in both Pacific and Atlantic Oceans find decadal and multidecadal variability (i.e., periods >10 yr) directly associated with ocean–atmosphere interaction (e.g., [Deser and Blackmon 1993](#); [Kushnir 1994](#); [Deser et al. 1996](#)). Modeling studies suggested that oceanic advection and/or Rossby wave propagation are candidates for the delayed-negative feedback mechanism responsible for the quasiperiodicity of the phenomenon (e.g., [Latif and Barnett 1994](#); [Miller et al. 1997](#); [White and Cayan 1998](#)).

In a much earlier study of the SST and sea level pressure (SLP) records, [Bjerknes \(1964\)](#) concluded that in the North Atlantic, decadal variability in SST was linked to that of the wind-driven subtropical gyre and associated poleward Gulf Stream heat transport. Later, [White and Barnett \(1972\)](#) proposed that, in the North Pacific, low frequency variability of upper ocean heat storage in the midlatitudes could produce decadal fluctuations in the overlying westerly wind regime. More recently, [Latif and Barnett \(1994\)](#) diagnosed a global ocean–atmosphere model simulation, and explained the 15–25-yr interdecadal variability in the North Pacific as resulting from variability in the western boundary current heat transport and middle latitude SST influence on the atmospheric circulation.

A transitional period in climate variability during the late 1970s attracted much attention, when a deeper Aleutian low, warmer SSTs in the eastern North Pacific, and cooler SSTs in the central and western middle latitudes replaced a persistent period of opposite conditions ([Nitta and Yamada 1989](#); [Trenberth 1990](#); [Ebbesmayer et al. 1991](#); [Trenberth and Hurrell 1994](#)). [Trenberth \(1990\)](#) and [Graham \(1994\)](#) called this transition a “climate shift.” Similar climate shifts were also observed in the early 1920s and mid-1940s ([Kondo 1988](#)). [Mann and Park \(1994\)](#) and [Zhang et al. \(1997\)](#) portrayed these climate shifts as part of a quasiperiodic interdecadal signal of 15–25-yr period.

Understanding the role of decadal and multidecadal variability in the Pacific Ocean in modulating SST and SLP anomaly patterns associated with the Southern Oscillation is also necessary for improving El Niño–Southern Oscillation (ENSO) prediction skills ([Balmaseda et al. 1995](#); [Chen et al. 1995](#); [Wang 1995](#); [Kirtman and Schopf 1997](#); [Latif et al. 1997](#)). For example, during the 1980s, predictive skill for ENSO was high, but in a recent equatorial warming of the Pacific ocean during the 1990s, ENSO’s predictive skill has dropped significantly ([Ji et al. 1996](#)). [Latif et al. \(1997\)](#) proposed that midlatitude interdecadal variability with tropical signatures modulates the ENSO signal. On the other hand, [Graham \(1994\)](#) and [Zhang et al. \(1997\)](#) proposed that interdecadal variability is a phenomenon, stemming from tropical–extratropical interaction.

The present study provides a detailed description of the upper ocean and lower atmosphere patterns associated with interdecadal variability in the Pacific basin and their joint evolution. In [section 2](#), data and methods, including the statistical techniques, are described. In [section 3](#), statistical results are presented. Discussion of results is found in [section 4](#). By following the evolution of covarying upper ocean temperature and SLP anomalies, we are able in [section 4](#) to compare our results with previous work and to propose mechanisms that could maintain the interdecadal signal against dissipation and account for its evolution around the Pacific basin.

## 2. Data and methods

In this study, the surface analysis utilizes two new global gridded datasets for monthly SST and SLP anomalies (1900–91). The SST data are based on the Hadley Center Global Ocean Surface Temperature Atlas (GOSTA) compilation from which observational biases have been removed ([Bottomley et al. 1990](#)). The data were subjected to an optimal smoother algorithm in a reduced space, generated through a principal component analysis, as described in [Kaplan et al. \(1998\)](#). The SLP data are based on the Comprehensive Ocean–Atmosphere Data Set compilation ([Woodruff et al. 1987](#)) and an optimal interpolation algorithm similar to the one used for SST ([Kaplan 1998](#), personal communication). The present analysis uses data over the Pacific basin only.

The subsurface analysis utilizes a subset of temperature profiles obtained from an ad hoc global observing system for 45 yr (1950–94). Approximately 1000–2000 temperature profiles were collected monthly during this period over the global ocean. The original dataset is composed of mechanical and expandable bathythermographs (MBTs, XBTs), as well as hydrographic temperature profiles. It has been subjected to rigorous quality control procedures at the Joint Environmental Data Analysis center at the Scripps Institution of Oceanography (SIO). Quality control procedures have been defined under guidelines provided by the Global Temperature–Salinity Project described by [White et al. \(1988\)](#). In this study we use only the XBT-based analysis from 1970 to 1994. From this dataset, heat content in the upper 400 m of the Pacific Ocean (HS) has been computed following [White \(1995\)](#).

To identify the dominant frequency in these three datasets and their temporal characteristics, complex empirical orthogonal function (CEOF) analysis is used ([Wallace and Dickinson 1972](#); [Barnett 1983](#); [Horel 1984](#)). Ideally, CEOF analysis technique enables one to isolate the evolutionary character of dominant signals without any a priori knowledge of their frequencies. Each component identified by the analysis is represented in terms of a spatial structure  $E(x, y)$  and an associated time dependent  $A(t)$ . Both  $E$  and  $A$  are complex and are thus written in terms of a phase [ $\epsilon(x, y)$ ,  $\Phi(t)$ ] and an amplitude [ $E(x, y)$ ,  $A(t)$ ]. The spatial evolution of the signal can then be reconstructed, through its full cycle, from a single CEOF. The real part of the product of  $E$  and  $A$  can be written as

$$z = A(t)E(x, y) \cos[\Phi(t) + \epsilon(x, y)].$$

If  $\Phi(t)$  is a linear function of time, the slope of the linear fit identifies the signal's period. In the present study the CEOF analysis is based on the covariance matrix of data. For HS, 12-month averages centered on January are used. For SST and SLP we use seasonal averages: November–March for winter and May–September for summer.

### 3. Results

The climatological background at the surface and subsurface is well documented in the literature and is not reproduced here ([Peixoto and Oort 1992](#); [White 1994](#); [White and Cayan 1998](#)). Major features in the annual mean HS distribution ([White 1994](#), his [Fig. 2b](#)) include tropical, subtropical, and subarctic circulation regimes. This derives from the physical relationship between computations for HS and steric sea level height from 400 m to the sea surface ([White and Tai 1995](#)). The western intensification of the subtropical gyre is associated with maximum HS values near 18°N between 130° and 150°E in the Philippine Sea. A countercurrent trough is found between 5° and 10°N with the eastward flowing North Equatorial Countercurrent on its equatorward side and the westward flowing North Equatorial Current (NEC) on its poleward side, mostly from 10°–15°N. Maximum HS gradient is found between 35° and 42°N from Japan to the date line, associated with Kuroshio–Oyashio Extension Currents.

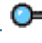
#### a. CEOF of SST and SLP anomalies for 1900–91

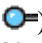
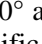
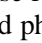
The CEOF is applied to seasonal SST and SLP anomalies during the interval 1900–91. The first SST CEOF (not shown) corresponds to the well-known ENSO mode (45% of total variance). The second SST CEOF (not shown, 14% of total variance) is associated with low-frequency variability with decadal timescales. This mode is not clearly separable ([North et al. 1982](#)) from consecutive CEOFs. However when the data is subjected to a tangent Butterworth low-pass filter with a cutoff at a period of 8 yr, the features of this decadal fluctuation become distinct and robust. In [Figs. 1](#) and [2](#), we show the separately analyzed SST and SLP first CEOFs modes (respectively) of the low-pass filtered cold season (November–March) anomalies. We show only the cold season results because of a lack of coherent atmospheric signal during the warm season. It is interesting to note that the SST first CEOF mode is only slightly changed during summer (see also [Trenberth and Hurrell 1994](#)). The summer SLP mode (not shown) is considerably weaker than its wintertime counterpart. The seasonal dependence of the SLP analysis implies that analysis of annually averaged surface data may lead to erroneous conclusions on the mutual relationship between the ocean and the atmosphere.

The first cold season SST CEOF pattern ([Fig. 1](#), top panel) represents 36% of the total low-pass variance. The CEOF is presented here in terms of its amplitude (contours and arrow length) and phase (arrow direction). The phase angle is measured in the clockwise direction with reference to an arbitrary starting point. For example, if at location A the arrow is pointing west, and at B north, then the implication is that the signal arrives later at B. If the temporal phase varies linearly with time, this 90° difference implies that the delay is ¼ of a period long.

[Figure 1](#) (top) clearly depicts the out-of-phase relationship between the central North Pacific and the northeast Pacific (180° differences in the phase vectors), as well as with the equatorial regions. In the central midlatitude region, large SST anomalies are found along the subarctic frontal zone (SAFZ) and near the Kuroshio bifurcation front ([Mizuno and White 1983](#); [Suga et al. 1997](#)) between 30° and 40°N. There is 20°–30° difference between the spatial phase angle along the SAFZ and that in the subtropical front region to the east-southeast. The phase difference can be translated into a time difference once the period of variability is defined (see below). The signal appears first along the SAFZ, and only then in the subtropical

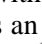
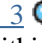
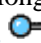

front region, consistent with [Nakamura et al. \(1997\)](#). Local maxima are present in the subtropics and along the northeast Pacific. Large SST anomalies are also found just west of 150°W and off shore of the Baja Peninsula. A rough symmetry is identified, in the eastern tropical Pacific, with maximum values on both sides of the mean position of the intertropical convergence zone at 25°N and 15°S and between 100° and 140°W. The distribution of the SST anomalies presented here closely resembles those obtained in the previous literature when Pacific decadal variability was studied (e.g., [Nitta and Yamada 1989](#); [Trenberth and Hurrell 1994](#); [Zhang et al. 1997](#)).

When the temporal amplitude and phase distributions are examined ([Fig. 1](#) , bottom) the very low-frequency nature of the signal is evident. Between 1900 and 1991, the temporal phase displays extended intervals of steady, linear evolution with time: 1901–13; 1921–32; 1935–52; 1954–63, and 1966–91. During these time intervals, the amplitude of the time coefficient is relatively large, and the slope of the phase indicates a period of 20–25 yr. In the intermediate years, the amplitude is much lower and the phase behavior less regular.

The first cold season SLP CEOF pattern ([Fig. 2](#) ) represents 55% of the total low-pass variance. Maximum variability is found to occur almost simultaneously between 40° and 60°N and between 150°W and the date line ([Fig. 2](#) , top). The pattern resembles the North Pacific pole of the Pacific–North America pattern ([Wallace and Gutzler 1981](#)). In addition, some eastward spreading of the signal, that is, a clockwise rotation of the phase vector over a limited angular sector, occurs between 40° and 50°N. The temporal amplitude and phase distributions with time ([Fig. 2](#) , bottom), agree relatively well with those corresponding to the low-pass SST CEOF in their indication of the intervals of large amplitude and linear phase evolution, as well as the suggested periods of the fluctuation. The distribution of SLP anomalies presented here resembles the distribution obtained by [Trenberth and Hurrell \(1994\)](#) and [Zhang et al. \(1997\)](#) when they examined the differences between the winter mean SLP for the most recent decades compared to earlier data. This pattern of interdecadal variability is associated with changes in the intensity and location of the Aleutian low. The wind stress during winter in the eastern Bering Sea is accordingly modified and could be correlated with interdecadal variations of the upper ocean biomass there, as identified by [Sugimoto and Tadokoro \(1998\)](#).

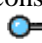

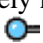
The simultaneity of the SLP and SST cycles from the 1970s onward (a period during which an adequate subsurface dataset is available) will be discussed in detail in [sections 3](#) and [4](#).

### *b. CEOF analysis of HS anomalies for 1970–94*

CEOF analysis is applied to the gridded HS anomalies computed from the XBT observations during the 1970–94 period. The first two CEOF patterns are well separated according to the [North et al. \(1982\)](#) criterion, and they represent 43% and 19% of the total variance, respectively. The first pattern is associated with ENSO (not shown) with maximum variability and an east–west seesaw structure along the equator. The second pattern is an interdecadal signal off the equator ([Fig. 3](#) , top), requiring approximately 20–25 yr to complete one full cycle ([Fig. 3](#) , bottom). In the North Pacific, maximum interdecadal variability extends from Japan to approximately 150°W, within the SAFZ and near the Kuroshio bifurcation front. Farther south, significant amplitude is located along the southern limit of the subtropical gyre as determined by the subsurface thermal structures ([White 1995](#), his [Fig. 2](#) ). A general clockwise rotation of the phase vector, when moving clockwise along the axis of maximum amplitude starting at 170°W ([Fig. 3](#) , top), indicates an anticyclonic propagation or spreading of the interdecadal signal from the high gradient region in the midlatitudes to the minimum gradient region in the subtropics. However, there are several regions (e.g., SAFZ) where the phase angle remains constant, indicating that in these regions HS evolution is stationary. We will return to this aspect in [section 4](#). Another local maximum is found east of the Philippine Sea, which corroborates results from [White and Tai \(1995\)](#). The links between the latter maximum and the strength of the subtropical gyre are still to be identified.

The second CEOF pattern also reveals HS anomalies in the western South Pacific Ocean, centered between 10° and 25°S, in phase with those in the SAFZ to the north. This anomaly can be seen propagating onto the equator just east of Australia and New Guinea (clockwise rotation of the phase vector while moving westward along the axis of maximum values), providing extratropical HS anomalies with direct access to the equatorial domain. This may arise from the intersection of the South Pacific subtropical gyre with the equator, as the North Pacific subtropical gyre is shielded from the equator by the Countercurrent Trough near 10°N.

### *c. Evolution of interdecadal HS anomalies for 1970–94*

The space–time evolution of HS anomalies is obtained by reconstructing the life cycle of the second CEOF pattern using the formulation explained in [section 2](#), and is displayed in [Fig. 4](#) . Here we present the evolution of the pattern through approximately half a cycle as in [Latif and Barnett \(1994, their Fig. 2](#) ) except that we use six frames (for easy comparison with [Fig. 7](#)  in [section 3d](#)), separated by 1/10th of a period from another (we arbitrarily set the period to be 20 yr). Note that years 0 and 10 are identical except for the polarity of the anomalies. The units of HS are also converted to °C m for comparison with the Latif and Barnett analysis. Year 0 roughly corresponds to the state of the field during winter 1970. In the North Pacific for approximately 2–4 yr (years 0 and 2) maximum positive HS anomalies appear and amplify in the middle

latitudes along the SAFZ between 30° and 45°N, from Japan to 150°W. Anomalies of opposite polarity are found along the eastern boundary and in the northern subtropics. As will become evident from the remaining panels, the latter are remnants of the previous half cycle of this pattern, and decay as the midlatitude anomaly intensifies. After that, anomalies at the eastern end of this domain near 150°W begin to spread south and then southwestward in the direction of the Philippine Archipelago (years 2 to 6). At the same time the midlatitude segment of the anomaly intensifies while becoming more narrowly confined in the SAFZ region and with some spreading westward along 35°N (year 6). In panel 5 (year 8), the main SAFZ anomaly is confined west of 160°E and weakens (year 10). In the subtropics, the anomaly is now strong, well-developed, and oriented southwest–northeast. East of the Philippine Sea a large anomaly has also developed and spreads northwestward and southward tracing the split in the NEC (years 8 and 10). Weaker anomalies extend to the North and Central American coastline (year 8). To the north they enter into the Gulf of Alaska (year 10). To the south, the anomalies along the coast of Mexico are in line with the path of the California Current (year 10, and years 2, 4, and 6 with opposite polarity). As the anomalies in the SAFZ weaken and those in the subtropics strengthen, weak anomalies of opposite polarity appear between these two regions at 30°N between 140°E and the date line (years 6 and 8).

The regions where the largest HS anomalies are found are generally compatible in amplitude with those of [Latif and Barnett \(1994\)](#), their [Fig. 2](#) (●). However, while the model anomaly centers maintain their relative strength and remain in opposite polarity throughout the “oscillation,” the observed anomaly centers do not. Moreover the model anomalies mostly appear to propagate northward over the central western subtropical gyre as anomalies of one sign displace those with opposite sign. This is not depicted by the observations. Compare for example our years 6 and 8 with Latif and Barnett’s years 5 and 7.5. In the present analysis, positive anomalies intensify and weaken between 30° and 45°N, with very little latitudinal displacement. In Latif and Barnett, a broad negative anomaly moves northward from the subtropics to displace the area of positive anomaly in the midlatitudes. Thus the present analysis does not show anomalies propagating from the subtropics to the midlatitudes and emphasizes the long lag (about 5 yr or almost ¼ of the cycle) between the timing of maximum amplitude in the SAFZ and in the subtropics. These differences will be further discussed in [section 4](#).

To the south the main path along which subtropical maximum HS anomalies are found is poleward of the surface manifestation of the NEC. However that path follows the shear flow of the NEC at 200–400-m depth as observed by [White and Cayan \(1998\)](#). This strongly suggests that this signal in anomalous HS derives from subsurface temperature anomalies formed and advected along the subsurface pathway of the subtropical gyre. The path to the subsurface must then begin east of the date line as proposed by [Watanabe and Mizuno \(1994\)](#) and [Deser et al. \(1996\)](#). When we follow positive HS anomalies, during years 4 to 10, they intensified along this subsurface pathway, but during years 10 to 14 (the latter is identical to year 4 with opposite polarity), they diminish steadily, disappear in year 14 and are replaced by HS anomalies of the opposite sign following the same subsurface pathway.

Using upper ocean temperature anomalies at standard depths from the surface to 400 m enables us to construct time–depth diagrams at three key locations along the path of maximum interdecadal HS anomalies, from the central SAFZ to the east of the Philippine Sea ([Fig. 5](#) ●). All the way down to 400 m, warm (unshaded) and cool (shaded) anomalies can be clearly identified.

In the northern section of the subtropical gyre which includes the central SAFZ ([Fig. 5](#) ●, top), the vertical structure of anomalous upper ocean temperature is uniform with depth, with maxima at 100 m, near the top of the mean depth of the main pycnocline. This is suggestive of the baroclinic response of the ocean to interdecadal change of wind stress curl forcing (e.g., [Miller et al. 1998](#)). Vertical mixing may also have played a role in maintaining this vertical uniformity over the mixed layer and the upper portion of the main pycnocline ([Miller et al. 1994](#)).

In the eastern section of the subtropical gyre, east of the SAFZ and straddling 150°W ([Fig. 5](#) ●, middle), downward propagation of the SST anomalies can be seen from 125 to 200 m. This is the location of North Pacific Central Mode Water (NPCMW, after [Suga et al. 1997](#)), and where [Qiu and Huang \(1995\)](#) identified mean detrainment (i.e., subduction) occurring at a rate of 25–50 m yr<sup>−1</sup>, associated with lateral induction. In the present study, the averaged subduction rate associated with interdecadal variability (i.e., the speed at which water is being renewed in the main pycnocline) is estimated to have been 10–15 m yr<sup>−1</sup>. These values are similar to those obtained by [Deser et al. \(1996\)](#), who found a similar downward propagation of interdecadal temperature anomalies in this region.

In the southern section of the subtropical gyre ([Fig. 5](#) ●, bottom), maximum values of upper ocean temperature anomalies occurred at 200 m, where they are out of phase with those at the sea surface (1970–76 and 1984–88). Not only does this support the subduction hypothesis, but it indicates that pycnocline temperatures were mostly decoupled from mixed layer temperatures over this portion of the subtropical gyre.

#### *d. Joint evolution of SST and SLP anomalies for 1970–94*

To determine the space–time evolution of the SST and SLP patterns associated with the second CEOF of HS, we project these fields onto the complex time series corresponding to that of the CEOF for the common time interval (1970–91). This

is done after augmenting the data series at each grid point by first adding to it its Hilbert transform (a procedure similar to the first stage of a CEOF analysis); second, multiplying these values by the complex conjugate of the normalized EOF time series, and finally dividing the result by the number of samples. The results, or SST and SLP projections, are displayed in [Fig. 6](#) (top and bottom, respectively). It should be noted that when the HS field is projected onto the complex SST and SLP time series patterns are very similar to those presented in [Fig. 3](#). Therefore, the temporal phase for the SST and SLP patterns are consistent with that of HS (by construction) and the casting of the interdecadal signal observed from the subsurface data in the context of the almost one century long surface record is robust. Moreover, the relative directions of the arrows in the three panels (HS at the top of [Fig. 3](#); SST and SLP in [Fig. 6](#)) are indicative of their mutual time lag relationship. For example, the HS maximum amplitude found in the SAFZ lags that of the SST by 1–2 yr ( $20^{\circ}$ – $30^{\circ}$  assuming a 20-yr cycle). In the eastern section of the subtropical gyre (where subduction occurs) HS lags by 3–4 yr the maximum SST anomaly in the SAFZ (i.e., a  $45^{\circ}$ – $60^{\circ}$  difference in the orientation of the phase vectors, and a clockwise rotation from SST to HS fields). The amplitude and the relative phase distribution captured in both projections are close to those found in the first CEOFs of the low-pass SST and SLP data, respectively, during the 1900–91 period ([Figs. 1](#) and [2](#)). The close resemblance between the CEOF patterns and the projections suggests that HS anomalies must have also evolved in parallel, in a manner depicted in [Fig. 4](#).

The projection of SST anomalies onto the time series of the first HS CEOF ([Fig. 6](#), top) displays maximum variability along the SAFZ and near the region of the NPCMW formation. These two key regions have also been identified by [Nakamura et al. \(1997\)](#). An out-of-phase relationship is found adjacent to the North American coastline. In the eastern Pacific, south of  $30^{\circ}$ N the anomalies spread westward as time progresses, following a path along the California current as it merges with the NEC southeast of the Hawaiian Archipelago. Relative symmetry can be found in both hemispheres, similar to that observed by [White and Cayan \(1998\)](#). The projection pattern for SLP anomalies ([Fig. 6](#), bottom) displays maximum variability north of  $40^{\circ}$ N northeast of the SAFZ, with a clear eastward propagation and amplification of the signal occurring between  $30^{\circ}$  and  $50^{\circ}$ N from Japan to  $140^{\circ}$ W. From there the signal gets weaker with a hint of southeastward expansion. This pattern is similar to that associated with interdecadal variability in the Aleutian low (e.g., [Namias et al. 1988](#); [Wang 1995](#)). The relative position of SST and SLP maxima in the North Pacific (SLP anomalies lying north-northeast of the SST anomalies) and its physical meanings will be discussed later.

To get more insight into the joint evolution of interdecadal SST and SLP anomalies and ocean–atmosphere interaction, we reconstruct these two fields from the projection patterns of [Fig. 6](#). The six frames that represent 10 yr of the simultaneous SST and SLP cycles, are displayed every 2 yr ([Fig. 7](#), years –4 to 6). The choice for the first year to be displayed is arbitrary but, in order to simplify the discussion in [section 4](#), we prefer to start 4 yr before the year chosen as 0 for the HS reconstruction (in [Fig. 4](#), the years are marked with reference to that choice). Individual panels are separated by a phase difference of  $\pi/5$  (or 2 yr in real time assuming a nominal 20-yr cycle). In this reconstruction the third panel (year 0) could also be thought of as representing the situation during the winter of 1970. In [Fig. 7](#), year –4 to year 6, clearly represents the evolution of positive (negative) SLP anomalies along  $40^{\circ}$ N from east of Japan toward the eastern Pacific (year –4). This evolution amounts to a weakening (strengthening) of the Aleutian low (year 2), with easterly (westerly) anomalies between  $25^{\circ}$  and  $40^{\circ}$ N and southerly (northerly) anomalies west of the date line and north of  $30^{\circ}$ N. This lead to the development of positive (negative) SST anomalies, most likely through ocean–atmosphere heat exchange ([Auaud et al., 1998](#)), and wind mixing and meridional Ekman transport anomalies ([Miller et al. 1994](#)). From year –4 to year –2 positive (negative) SST anomalies are found to originate from the Alaskan gyre and to merge with weaker anomalies of the same polarity, which originated from  $30^{\circ}$ N between  $140^{\circ}$ E and the date line. During years 0 and 4, a relatively stable and narrow pattern of large positive (negative) SST anomalies is centered on the SAFZ stretching from Japan to  $140^{\circ}$ W. The SST anomaly partly underlies the larger pattern of positive (negative) SLP anomaly, the latter having its maximum north-northeast of the SST anomaly (north of  $40^{\circ}$ N, between  $170^{\circ}$ E and  $140^{\circ}$ W). A similar relative geometry was found in the midlatitude Atlantic Ocean by [Palmer and Sun \(1985\)](#). The SST anomaly pattern displayed here is similar to that observed by [Tanimoto et al. \(1993\)](#) and is consistent with Sverdrup dynamics ([Miller et al. 1997](#)). The strongest zonal anomalous SLP gradient is seen in the vicinity of the maximum SST anomalies (years 0, 2, and 4). During this part of the cycle, a distinct maximum of SST anomalies occurs to the east between  $30^{\circ}$  and  $40^{\circ}$ N and between  $140^{\circ}$  and  $160^{\circ}$ W, in the vicinity of the NPCMW formation region ([Nakamura et al. 1997](#)). Here decadal changes in heat flux divergence must dominate in the Ekman layers ([Yasuda and Hanawa 1997](#)), and lateral induction and vertical subduction are known to occur (e.g., [Qiu and Huang 1995](#)). Thereafter the transition from one phase of the cycle to the other takes approximately 3–4 yr to complete (year 6, and the negative of year –2). While the SLP anomaly weakens in a southeast direction (years 4 and 6) it is replaced by a weak negative (positive) SLP anomaly that first appears off Japan, and then spreads eastward along the SAFZ toward the North American coastline (year –2 with opposite polarity). These changes in SLP are accompanied by a weakening of the SST anomaly as it narrows down, to clearly demarcate the SAFZ and the subtropical gyre subduction region north of the Hawaiian Archipelago (year 4).

Along the northern and eastern Pacific Ocean rims, the patterns are characterized by SST anomalies in opposite polarity to those in the central ocean basin. An intensification of SST anomalies occurs from the Gulf of Alaska to the Kamchatka Peninsula accompanied by a southward expansion ([Fig. 7](#), years 0–6). The anomalies make their way into the central ocean basin during the following half “cycle” ([Fig. 7](#), year –2 with opposite polarity). A south-southwestward expansion of subtropical SST anomalies also occurs from the Baja Peninsula south of  $30^{\circ}$  to  $10^{\circ}$ N and  $140^{\circ}$ W (years 2–6 and year –2 with opposite polarity).

A mirror image of the Northern Hemisphere tropical SST anomalous pattern develops and grows in the Southern Hemisphere between South America and 140°W with maximum along 15°S (years 2 to 4) as noted by [White and Cayan \(1998\)](#).

#### 4. Discussion and conclusions

The evolution of interdecadal HS anomalies is clearly centered on the subtropical gyre region. At the surface the SST anomaly pattern is basin wide, with extremes in the subtropical and subarctic gyres, along the northern and eastern ocean boundary, and in the Tropics. While the SLP anomaly pattern is mainly confined to the Aleutian low region, small changes also occur in the SLP and SST anomaly patterns in the tropical Pacific when weak tropical SST anomalies change polarity ([Fig. 7](#) ●, years -2 and 0). The tropical SLP anomalies are such that the Southern Oscillation index (SOI) must be modulated accordingly, yielding a possible contribution of interdecadal SLP anomalies to low-frequency variability of ENSO. SST anomalies indeed intensify along the equator with maximum values between 150°E and 170°W (years 4–6). From 1982 until 1989 the tropical SLP interdecadal signal could have contributed to a weakening of the trade winds. ENSO events were then remarkably well formed in both magnitude and periodicity and relatively more predictable as compared to the 1990s ([Ji et al. 1996](#)).

For the past 92 years the interdecadal variability in the North Pacific is “quasiperiodic.” It also represents a coevolution among the oceanic and atmospheric variables. As such its evolution can be broken down into four relatively distinct phases (each 2–4 yr long) throughout its 20–25-yr cycle: the onset phase (years -4 and 2, [Fig. 7](#) ●), the growth phase (years 0 and 2, [Fig. 7](#) ●), the decay phase (years 4 and 6, [Fig. 7](#) ●), and the return phase (years -4 and -2 with opposite polarity, [Fig. 7](#) ●). The onset phase is a transition phase, marked by the slow eastward evolution of relatively weak covarying SST and SLP anomalies from the western ocean to the eastern ocean. The growth phase in both surface fields is a stationary phase, with rapid growth in SST and SLP anomalies occurring in the central North Pacific Ocean, leading to maximum magnitudes there. The decay phase in both surface fields is transitional, marked by evolution of covarying SST and SLP anomalies away from the region of maximum SST and SLP variability.

The return phase for the “warm” part of the cycle occurs at the same time as the onset phase for the “cold” part of the cycle. As such, the growth phase may establish conditions that not only initiates the decay of the warm phase but heralds the onset of the cold phase. In the reconstruction presented in [Fig. 7](#) ● (years -4 and -2), weak North Pacific SST anomalies converge into the SAFZ from the Gulf of Alaska, and the region southeast of Japan (30°N and between 140°E and the date line). The southward movement of SST anomalies from the Alaskan gyre into the SAFZ region could be associated with variability in the volume transport of the gyre identified by [Lagerloef \(1995\)](#). The possibility exists that the weak anomalies of the return phase, in opposite polarity to the large SAFZ anomalies during the previous half cycle, could trigger the new onset phase (e.g., through an atmospheric response as argued by [Latif and Barnett 1994, 1996](#)). If the atmosphere responds to these anomalies through an anomalous anticyclonic (cyclonic) wind stress curl in the middle ocean basin, it could enhance positive (negative) SST and HS anomalies west of 140°W ([Miller et al. 1998](#)). A more quantitative analysis that compares the growth of the anomalies with surface heat and momentum fluxes could shed more light on this issue.

The evolution of HS anomaly in the central North Pacific agrees with the subduction of mixed layer thermal anomalies in the NPCMW area ([Yasuda and Hanawa 1997; Qiu and Huang 1995](#)) and subsequent formation of anomalous subsurface temperature by the subtropical gyre at 200–400 m. The average speed of the subduction is found to be 0.01–0.03 m s<sup>-1</sup> as in [Deser et al. \(1996\)](#). The SST anomaly evolution in the vicinity of the Hawaiian Archipelago (subtropical front region, [Nakamura et al. 1997](#)) is consistent with the advection of SST anomalies around the subtropical gyre with the surface geostrophic flow. Such evolution could be maintained against dissipation by local positive feedback deriving from the covarying SLP anomaly pattern ([White and Cayan 1998](#)).

The subtropical front region is the only place where systematic propagation of the upper ocean thermal anomalies is detected in our analysis. As discussed in the previous section, we do not observe systematic propagation around the entire subtropical gyre as depicted in [Latif and Barnett \(1994, 1996\)](#). We could also not detect variations along the western boundary current, indicative of a delayed-negative feedback effect on the midlatitudes associated with the covarying SST, SLP interdecadal anomalies. It is possible that the data do not capture the western boundary current phenomenon due to the sparsity of the observations or horizontal resolution. Latif and Barnett could have simulated interdecadal variability through what appears to be extratropical Rossby waves propagation. From our diagnostic analysis, the role of changes in the heat transport by the Kuroshio Current as a viable delayed-negative feedback mechanism responsible for quasiperiodicity in interdecadal variability in the North Pacific basin remains in question.

We interpret our results as indicative of the change in the character of the subtropical gyre, brought about by a combined process of subduction and wind-stress-induced circulation changes. Note that in the decay phase of the cycle ([Fig. 4](#) ●, years 6 and 8) HS anomalies of the same polarity are arranged in a horseshoe pattern around the subtropical gyre, while opposite sign anomalies appear in the middle. It is well known that in a north–south cross section of the midlatitude ocean

temperature field, the isotherms trace a “bowl” shaped pattern, with the warmest temperatures located in the center of the subtropical gyre. Noting that the HS field is calculated between a depth of 400 m and the surface, the pattern in [Fig. 4](#) (years 6 and 8) is consistent with the north–south spreading and shallowing of this isothermal bowl during the warm half cycle, and the narrowing and deepening of the bowl in the cold half cycle. In the same [Fig. 4](#), we also note that the SLP field, during the years leading to the decay phase, indicates a wind-stress curl anomaly over the central ocean region that would induce upward (downward) Ekman pumping in the warm (cold) half cycle. This is consistent with the vertical displacement of the isotherms as discussed above. A more quantitative analysis is needed. Indeed, recent work by [Deser et al. 1996](#) (personal communication) confirms our assertion through a quantitative analysis based on wind stress data.

At the surface, warm anomalies in the SAFZ are followed with some delay (about 1 yr) with the appearance of cold anomalies along the North American seaboard, which then spread westward and into the Tropics, As suggested by [Trenberth and Hurrell \(1994\)](#), [Graham \(1994\)](#), and [Zhang et al. \(1997\)](#) these anomalies could feed back positively on the midlatitude atmospheric circulation, enhancing the year-to-year persistence of the weaker Aleutian low to the north. This positive feedback will work in the opposite phase when the Aleutian Low is stronger than normal, midlatitude SSTs are cold and tropical SSTs are warm. Notably, during the last century the SST record does not always follow a full interdecadal cycle such as it did during the last two and a half decades ([Fig. 1](#), lower panel). It could be that what we are watching is a weak tropical–extratropical feedback loop that accounts for the persistence of anomalies in the Aleutian low region (from one winter season to the next) but is not enough to withstand the chaotic variability of the midlatitudes. Hence the phenomenon decays and reemerges after some delay with an arbitrary phase with respect to the previous appearance. However, such a mechanism could only explain the interannual persistent SLP anomalies but not the timescale of the phenomenon observed in the SST and HS analyses ([Figs. 1](#) and [3](#)) and in that of SLP ([Fig. 2](#)).

### Acknowledgments

Yves Tourre and Yochanan Kushnir are supported by NOAA Grant (UCSIO-10775411D/NA47GPO-188). Warren White is supported by NASA Grant (NA27GPO-539), and by NOAA Grant (NA47GPO-188-MOD3). We thank Drs. Art Miller (SIO) and Richard Kleeman (visiting scientist at the International Research Institute at LDEO) for the fruitful discussions we had with them. Data were processed by Dmitry Pozdnyakov.

---

## REFERENCES

- Auad, G., A. J. Miller, and W. B. White, 1998: Simulation of heat storage and associated heat budgets in the Pacific Ocean: Part 2. Interdecadal time scales. *J. Geophys. Res.*, **103**, 27 621–27 635.
- Balmaseda, M. A., M. K. Davey, and D. L. T. Anderson, 1995: Decadal and seasonal dependence of ENSO prediction skill. *J. Climate*, **8**, 2705–2715. [Find this article online](#)
- Barnett, T. P., 1983: Interaction of the monsoon and Pacific trade wind systems at interannual time scales. Part I: The equatorial zone. *Mon. Wea. Rev.*, **111**, 756–773. [Find this article online](#)
- Bjerknes, J., 1964: Atlantic air–sea interaction. *Advances in Geophysics*, H. E. Landsberg and J. van Mieghem, Eds., Academic Press, 1–82.
- Bottomley, M., C. K. Folland, J. Hsiung, R. E. Newell, and D. E. Parker, 1990: *Global Ocean Surface Temperature Atlas*. Joint Meteorological Office/MIT project. United Kingdom Dept. of Energy and Environment, HSMO, 20 pp, 313 plates.
- Chen, D., S. E. Zebiak, A. J. Busalacchi, and M. A. Cane, 1995: An improved procedure for El Niño forecasting: Implications for predictability. *Science*, **269**, 1699–1702.
- Deser, C., and M. L. Blackmon, 1993: Surface climate variations over the North Atlantic Ocean during winter: 1900–1989. *J. Climate*, **6**, 1743–1753. [Find this article online](#)
- , A. Alexander, and M. S. Timlin, 1996: Upper-ocean thermal variations in the North Pacific during 1970–1991. *J. Climate*, **9**, 1840–1855. [Find this article online](#)
- Ebbesmeyer, C. C., D. R. Cayan, D. R. McLain, F. H. Nichols, D. H. Peterson, and K. T. Redmond, 1991: 1976 step in the Pacific climate: Forty environmental changes between 1968–1975 and 1977–1984. *Proc. Seven Annual Pacific Climate (PACLIM) Workshop*, Pacific Grove, CA, California Department of Water Resources/Interagency Ecological Studies Program, 115–123.
- Folland, C. K., D. E. Parker, and F. E. Kates, 1984: Worldwide marine temperature fluctuations 1856–1981. *Nature*, **310**, 670–673.
- Graham, N. E., 1994: Decadal-scale climate variability in the tropical and north Pacific during the 1970s and 1980s: Observations and



Horel, J. D., 1984: Complex principal component analysis: Theory and examples. *J. Climate Appl. Meteor.*, **23**, 1660–1673..

Ji, M., A. Leetmaa, and V. E. Kousky, 1996: Coupled models predictions of ENSO during the 1980s and the 1990s at the National Centers for Environmental Prediction. *J. Climate*, **9**, 3105–3120.. [Find this article online](#)

Kaplan, A., M. A. Cane, Y. Kushnir, C. Clement, M. B. Blumenthal, and B. Rajagopalan, 1998: Analysis of global sea surface temperature 1856–1991. *J. Geophys. Res.*, **103**, 18 567–18 589..

Kawamura, R., 1994: A rotated EOF analysis of global sea surface temperature variability with interannual and interdecadal scales. *J. Phys. Oceanogr.*, **24**, 707–715.. [Find this article online](#)

Kirtman, B. P., and P. S. Schopf, 1997: Decadal variability in ENSO predictability and prediction. COLA Studies Rep. 43, 43 pp. [Available from COLA Studies, 4041 Powder Mill Road, Calverton, MD 20705.]

Kondo, J., 1988: Volcanic eruptions, cool summers and famines in the northeastern part of Japan. *J. Climate*, **1**, 775–788.. [Find this article online](#)

Kushnir, Y., 1994: Interdecadal variations in the North Atlantic sea surface temperature and associated atmospheric conditions. *J. Climate*, **7**, 141–157.. [Find this article online](#)

Lagerloef, G. S., 1995: Interdecadal variations in the Alaska Gyre. *J. Phys. Oceanogr.*, **25**, 2242–2258.. [Find this article online](#)

Latif, M., and T. P. Barnett, 1994: Causes of decadal variability over the North Pacific and North America. *Science*, **266**, 634–637..

—, and —, 1996: Decadal climate variability over the North Pacific and North America: Dynamics and predictability. *J. Climate*, **9**, 2408–2423.. [Find this article online](#)

—, R. Kleeman, and C. Eckert, 1997: Greenhouse warming, decadal variability, or El Niño? An attempt to understand the anomalous 1990s. *J. Climate*, **10**, 2221–2239.. [Find this article online](#)

Mann, M. E., and J. Park, 1994: Global scale modes of surface temperature variability on interannual to century time scales. *J. Geophys. Res.*, **99**, 25 819–25 833..

—, —, and R. S. Bradley, 1995: Global interdecadal and century-scale climate oscillations during the past five centuries. *Nature*, **378**, 266–270..

Miller, A. J., D. R. Cayan, T. P. Barnett, N. E. Graham, and J. M. Oberhuber, 1994: Interdecadal variability of the Pacific Ocean: Model response to observed heat flux and wind stress anomalies. *Climate Dyn.*, **9**, 287–302..

—, —, and W. B. White, 1998: A westward-intensified decadal change in the North Pacific thermocline and gyre-scale circulation. *J. Climate*, **11**, 3112–3127.. [Find this article online](#)

Mizuno, K., and W. B. White, 1983: Annual and interannual variability in the Kuroshio Current System. *J. Phys. Oceanogr.*, **13**, 1847–1867.. [Find this article online](#)

Nakamura, H., G. Lin, and T. Yamagata, 1997: Decadal climate variability in the North Pacific during the recent decades. *Bull. Amer. Meteor. Soc.*, **78**, 2215–2225.. [Find this article online](#)

Namias, J., X. Yuan, and D. R. Cayan, 1988: Persistence of North Pacific sea surface temperature and atmospheric flow patterns. *J. Climate*, **1**, 682–703.. [Find this article online](#)

Nitta, T., and S. Yamada, 1989: Recent warming of tropical sea surface temperature and its relationship to Northern Hemisphere circulation. *J. Meteor. Soc. Japan*, **67**, 375–383..

North, G. R., T. L. Bell, R. F. Cahalan, and F. J. Moeng, 1982: Sampling errors in the estimation of empirical orthogonal functions. *Mon. Wea. Rev.*, **110**, 699–706.. [Find this article online](#)

Oort, A. H., Y. H. Pan, R. W. Reynolds, and C. F. Ropelewski, 1987: Historical trends in the surface temperature over the oceans based on COADS. *Climate Dyn.*, **2**, 29–38..

Palmer, T. N., and Z. Sun, 1985: A modeling and observational study of the relationship between sea surface temperature in the north-west Atlantic and the atmospheric general circulation. *Quart. J. Roy. Meteor. Soc.*, **111**, 947–975..

Peixoto, J. P., and A. H. Oort, 1992: *Physics of Climate*. AIP Press, 520 pp..

Qiu, B., and R. X. Huang, 1995: Ventilation of the North Atlantic and North Pacific: Subduction versus obduction. *J. Phys. Oceanogr.*, **25**, 2374–2390.. [Find this article online](#)

Suga, T., Y. Takei, and K. Hanawa, 1997: Thermostat distribution in the North Pacific subtropical gyre: The central mode water and the subtropical mode water. *J. Phys. Oceanogr.*, **27**, 140–152.. [Find this article online](#)

Sugimoto, T., and K. Tadokoro, 1998: Interdecadal variations of plankton biomass and physical environment in the North Pacific. *Fish. Oceanogr.*, **7**, 289–299..

Tanimoto, Y., N. Iwasaka, K. Hanawa, and Y. Toba, 1993: Characteristic variations of sea surface temperature with multiple time scales in the North Pacific. *J. Climate*, **6**, 1153–1160.. [Find this article online](#)

Trenberth, K. E., 1990: Recent observed interdecadal climate changes in the Northern Hemisphere. *Bull. Amer. Meteor. Soc.*, **71**, 998–993.. [Find this article online](#)

—, and J. W. Hurrell, 1994: Decadal atmosphere–ocean variations in the Pacific. *Climate Dyn.*, **9**, 303–319..

Wallace, J. M., and R. E. Dickinson, 1972: Empirical orthogonal representation of time series in the frequency domain. Part I: Theoretical considerations. *J. Appl. Meteor.*, **11**, 887–892.. [Find this article online](#)

—, and D. S. Gutzler, 1981: Teleconnections in geopotential height field during the Northern Hemisphere winter. *Mon. Wea. Rev.*, **109**, 784–812.. [Find this article online](#)

Wang, B., 1995: Interdecadal changes in El Niño onset in the last four decades. *J. Climate*, **8**, 267–285.. [Find this article online](#)

Watanabe, T., and K. Mizuno, 1994: Decadal changes of the thermal structure in the north Pacific. *Int. WOCE Newslett.*, **15**, 10–13..

White, W. B., 1994: Slow El Niño oscillation boundary waves. *J. Geophys. Res.*, **99**, 737–22 751..

—, 1995: Design of a global ocean observing system for gyre scale in upper ocean temperature. *Progress in Oceanography*, Vol. 36, Pergamon, 169–217..

—, and T. P. Barnett, 1972: A servomechanism in the ocean–atmosphere system of the midlatitude North Pacific. *J. Phys. Oceanogr.*, **2**, 372–381.. [Find this article online](#)

—, and C.-K. Tai, 1995: Inferring interannual changes in global heat storage from TOPEX altimetry. *J. Geophys. Res.*, **100**, 24 943–24 954..

—, and D. R. Cayan, 1998: Quasi-periodicity and global symmetries in interdecadal upper-ocean temperature variability. *J. Geophys. Res.*, **103**, 21 335–21 354..

—, S. E. Pazan, G. W. Withee, and C. Noe, 1988: Joint Environmental Data Analysis (JEDA) Center for the scientific quality control of upper ocean thermal data in support of TOGA and WOCE. *Eos, Trans. Amer. Geophys. Union*, **69**, 122–123..

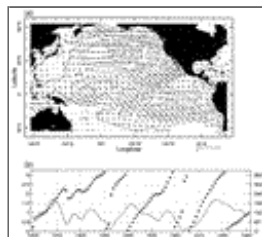
Woodruff, S. D., R. J. Slutz, R. L. Jenne, and P. M. Steurer, 1987: A comprehensive ocean–atmosphere dataset. *Bull. Amer. Meteor. Soc.*, **68**, 1239–1250.. [Find this article online](#)

Yasuda, T., and K. Hanawa, 1997: Decadal changes in the mode waters in the mid latitude North Pacific. *J. Phys. Oceanogr.*, **27**, 858–870.. [Find this article online](#)

Zhang, Y., J. M. Wallace, and D. S. Battisti, 1997: ENSO-like interdecadal variability: 1900–93. *J. Climate*, **10**, 1004–1020.. [Find this article online](#)

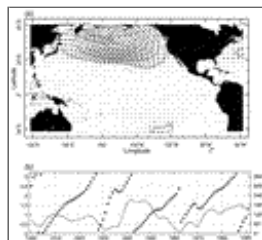
---

## Figures



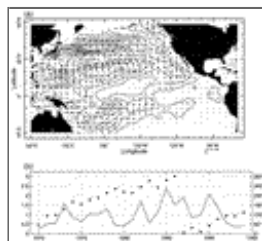
Click on thumbnail for full-sized image.

Fig. 1. Top: First CEOF pattern (36% of total variance) of filtered SST for 1900–91. The data is low-pass filtered using an 8-yr cutoff Butterworth filter. The amplitude of the anomalies are in  $^{\circ}\text{C}$ . The vectors represent the phase of the anomalies as well as their amplitudes. An eastward displacement associated with a clockwise rotation of the phase, indicates an eastward propagation of the signal. Bottom: The normalized temporal coefficient (amplitude in solid line and phase in solid circles) of the CEOF pattern above. The angles of the phase are displayed to the right.



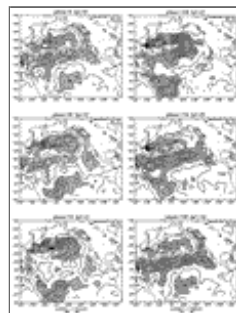
[Click on thumbnail for full-sized image.](#)

Fig. 2. Top: First CEOF pattern (55% of total variance) of winter SLP for 1900–91. The data is lowpassed using an 8-yr cutoff Butterworth filter. The amplitude of the anomalies are in mb. The vectors represent the phase of the anomalies as well as their amplitudes. The propagation convention is the same as in Fig. 1. Bottom: The normalized temporal coefficient (amplitude in solid line and phase in solid circles) of the CEOF pattern above. The angles of the phase are displayed to the right.



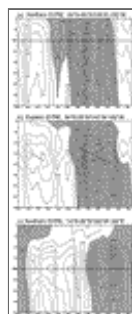
[Click on thumbnail for full-sized image.](#)

Fig. 3. Top: Second CEOF pattern of January centered 12-month averaged 0–400-m heat content anomalies (HS) for 1970–94. The mode explains 19% of the total variance. The amplitude of the anomalies is in  $10^9 \text{ J m}^{-2}$ . The vectors represent the phase of the anomalies as well as their amplitudes. The propagation convention is the same as in Fig. 1. Bottom: Time evolution of the second CEOF pattern of HS. The solid line indicates the time amplitude and the dots indicate the phase. The angles of the phase are displayed to the right.



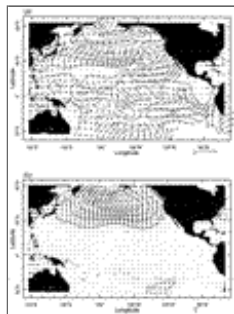
[Click on thumbnail for full-sized image.](#)

Fig. 4. Reconstructed space–time evolution of 10 yr of the interdecadal half cycle, obtained from the second CEOF mode of HS (units are in  $^{\circ}\text{C m}$ , with contours every 30 units). Solid contours (dashed contours) represent positive (negative) anomalies. Areas with absolute values larger than  $30^{\circ}\text{C m}$  are shaded. All frames which represent Januarys are separated by 2 yr starting from year 0 to year 10.



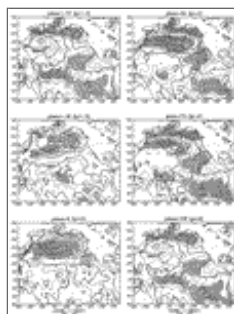
[Click on thumbnail for full-sized image.](#)

Fig. 5. Averaged Hövmoller diagrams of the temperature anomalies ( $^{\circ}\text{C}$ ) at depth associated with the interdecadal signal in the subtropical gyre. The three sections of the gyre are determined from the spatial distribution of the HS interdecadal signal in Fig. 4. The northern section (top), eastern section (middle), and southern section (bottom) represent averaged anomalies during 25 yr (1970–94). Negative anomalies are shaded. Horizontal black solid lines (top and bottom) represent depth at which anomalies are maximum. Slanted black solid lines (middle) represent maximum anomalies for the warm and cold events (respectively) during the 1970–94 period.



[Click on thumbnail for full-sized image.](#)

Fig. 6. Top: Projection of cold season mean SST data (Nov–Mar) against the second CEOF mode for HS, and for the joint period 1970–91. The amplitude of the SST anomalies are in  $^{\circ}\text{C}$ . The vectors represent the phase of the anomalies as well as their amplitudes. An eastward displacement associated with a clockwise rotation of the phase, indicates an eastward propagation of the signal. Bottom: Projection of cold season mean SLP data (Nov–Mar) on the CEOF second mode for HS, and for the joint period 1970–91. The amplitude of the SLP anomalies are in mb. The vectors represent the phase of the anomalies as well as their amplitudes. The propagation convention is the same as in Fig. 1.



[Click on thumbnail for full-sized image.](#)

Fig. 7. Reconstruction of the joint evolution of cold season SST, SLP anomalies corresponding to half a cycle of the interdecadal signal (from year  $-4$  to year 6). The evolution is obtained by projecting the original SST and SLP datasets on the CEOF second mode for HS, and for the period 1970–91. The amplitude for SST anomaly (thin solid lines and thin dashed lines for positive and negative anomalies respectively) is in  $^{\circ}\text{C}$  every  $0.1^{\circ}\text{C}$ . Areas with absolute values larger than  $0.2^{\circ}\text{C}$  are shaded. The amplitude of SLP anomaly (thick solid contours and thick dashed contours for positive and negative anomalies, respectively) is in mb every 0.5 mb.

\* Lamont-Doherty Earth Observatory Contribution Number 5834

Corresponding author address: Dr. Yves M. Tourre, Lamont-Doherty Earth Observatory, Columbia University, Palisades, NY 10964.

E-mail: [tourre@iri.ldeo.columbia.edu](mailto:tourre@iri.ldeo.columbia.edu)

top ▲



© 2008 American Meteorological Society [Privacy Policy and Disclaimer](#)

Headquarters: 45 Beacon Street Boston, MA 02108-3693

DC Office: 1120 G Street, NW, Suite 800 Washington DC, 20005-3826

[amsinfo@ametsoc.org](mailto:amsinfo@ametsoc.org) Phone: 617-227-2425 Fax: 617-742-8718

[Allen Press, Inc.](#) assists in the online publication of AMS journals.

